Powder Technology 399 (2022) 117098

Contents lists available at ScienceDirect

Powder Technology

journal homepage: www.elsevier.com/locate/powtec

Dual-wavelength extinction rainbow refractometry for *in-situ* characterization of colloidal droplets

Can Li [a,b], Qimeng Lv [b], Ning Li [a], Yingchun Wu [b], Xuecheng Wu [b,*], Chunsheng Weng [a], Cameron Tropea [c]

[a] National Key Laboratory of Transient Physics, Nanjing University of Science and Technology, 210094 Nanjing, China
[b] State Key Laboratory of Clean Energy Utilization, Zhejiang University, 310027 Hangzhou, China
[c] Institute of Fluid Mechanics and Aerodynamics, Technische Universität Darmstadt, 64287 Darmstadt, Germany

ARTICLE INFO

Article history:
Received 16 October 2021
Received in revised form 23 December 2021
Accepted 28 December 2021
Available online 3 January 2022

Keywords:
Colloidal suspension droplet
Rainbow refractometry
In situ multi-parameter characterization
Nanoparticle size and concentration
Extinction

ABSTRACT

Considerable interest and demand exists in multi-parameter characterization of colloidal droplets. However, an optical *in-situ* characterization of such droplets is a particular challenge due to its heterogeneous and multi-scale nature, motivating the investigation of a dual-wavelength extinction rainbow refractometry. An analytical model is proposed, in which dual-wavelength extinction effect of the inclusions on the amplitude of the primary rainbow peak allows measurement of inclusion concentration and particle size. The rainbow pattern itself yields the refractive index and diameter of the host droplet. Validation experiments using deionized monodisperse water droplets containing standard polystyrene nanoparticles with different concentrations (0%, 0.1%, 0.2%, 0.3%) and particle sizes (210 nm, 530 nm) were conducted. Measured refractive indices and droplet diameters agree well with the known values. Measurement errors of inclusion concentration and size were analyzed with and without *a prior* knowledge of the inclusion size. Measurement limits of this approach are also discussed.

1. Introduction

Droplets (host droplet) containing immiscible nanoparticles (inclusions), called colloidal droplets, are encountered in a wide variety of scientific and engineering applications: nanofluid fuels, spray drying, spray coating (painting), cooling, etc. For instance, the addition of metallic nanoparticles to conventional hydrocarbon liquid fuels to prepare nanofluid fuels is of considerable importance in enhancing thermophysical properties, increasing energy density, improving ignition and combustion characteristics, and reducing pollutant emissions of the base fuels [1]. The solubility of food and pharmaceutical powders depends on the solid phase particle concentration of the atomized colloidal droplets in spray drying [2]. To achieve efficient cooling, solid insoluble particles of different sizes and concentrations are added to the cooling droplet, enhancing its heat transfer capacity [3]. To correctly design and control the atomization process, it is necessary to know what concentration of inclusions are contained in the colloidal droplet and the correlation between the droplet diameter and the concentration of inclusions during the subsequent evaporation and combustion process [4–6]. Hence, a diagnostic tool for measurement of these quantities is highly desirable.

The optical measurement of colloidal droplets according to the size and refractive index of the host droplet, and the concentration and size of the inclusions has been a long-standing challenge due to several reasons: (1) colloidal droplets are heterogeneous and multi-scale in size (micron sized host droplet, nano sized inclusions); (2) a simultaneous measurement of both the liquid and solid phases is necessary for a complete description of the process; (3) an *in-situ* measurement of droplets in a flow (up to 100 m/s) is much preferred to an off-line sampling measurement, for example by scanning and transmission electron microscopy (SEM, TEM), atomic force microscopy, scanning probe microscopy, dynamic light scattering or with electrospray-scanning mobility particle sizer [7]. Optical measurement techniques have the advantages of being non-invasive, highly accurate and often capable of *in-situ* measurements. However, conventional droplet optical measurement techniques such as the phase Doppler technique (PD), forward small angle scattering (diffraction based techniques), interferometric particle imaging (IPI), etc. [8], are mostly based on the light scattering theory of homogeneous droplets. Although there exists accurate numerical methods for describing light scattering of colloidal droplets, such as T-matrix and DDA [9,10], they are practically only applicable to sub-micron colloidal droplets due to insufficient computing power. More recently the light scattering from colloidal droplets has been examined in detail in conjunction with the time-shift technique, and this represents an alternative approach to that followed in the present study [11,12].

Alternatively, empirical models to describe light scattering from drops containing single particles have been presented [13,14]; however, these lack a theoretical basis and are of limited applicability. Considerable work has been performed on stationary colloidal droplets, for instance the influence of inclusions on evaporation rate [15], burning rate [16], and induced velocity fields within the droplet [17]. Combining high-speed imaging and infrared thermography for temperature

* Corresponding author.
E-mail address: wuxch@zju.edu.cn (X. Wu).

https://doi.org/10.1016/j.powtec.2021.117098
0032-5910/

measurements, Pandey et al. [18] experimentally studied the evaporation and secondary fragmentation atomization of suspended fuel droplets (initial diameter: 300–500 μm) containing different concentrations (0–0.5% wt) of nanoparticles. Digital holography enabled the measurement of size and 3D position of the inclusion within a single millimeter sized droplet [19], but this method requires large host droplets. For a micron sized droplet stream, Wriedt et al. [20] retrieved droplet diameter and inclusion concentration respectively from the angular spacing and the slope of the scattering light distribution at a specific angular position of the colloidal droplet; the same group later used continuous wavelet transform to extract the inclusion number concentration, and estimated the inclusion size by intricately combining speckle image analysis and turbidity measurement [21]. Recently, the time-shift technique yielded inclusion concentration [22] and size [11] from the attenuation of the amplitude ratio between zero-order ($p = 0$) reflection and second-order ($p = 2$) refraction signals arising from the same illuminating Gaussian beam, focused much smaller than the droplet diameter. Here the index p refers to the number of paths a ray traverses in the droplet before exiting.

Despite the wide variety of techniques presented, most can only acquire partial information. Few techniques can simultaneously characterize the liquid and solid phase parameters of colloidal droplets, specifically the refractive index of the host droplet, inclusion size and concentration. However, simultaneous measurement of these quantities is desirable, since refractive index related droplet temperature or composition concentration is a critical parameter in heat and mass transfer between the droplet and its surroundings. Moreover, the inclusion size and concentration clearly affect the physicochemical properties (such as viscosity, surface tension, rheology, thermal conductivity, reactivity and catalytical ability) of colloidal droplets [23,24].

This then motivates the present study based on a dual-wavelength extinction rainbow refractometry (DERR) in which the dual-wavelength extinction of intensity ratio $I_{p=2}/I_{p=0}$ of the $p = 2$ and $p = 0$ rays is employed to retrieve inclusion concentration and size, while the conventional rainbow signal yields refractive index and diameter of host droplet. Rainbow refractometry (RR), first proposed by Roth et al. [25], has attracted attention for allowing *in-situ* measurement of size [26], non-sphericity [27], refractive index (temperature) [28,29], mixing ratio [30], transient evaporation rate [31,32], surface tension and viscosity [33,34] of the droplet. Similar to the extinction method and time-shift technique, the intensity of the $p = 2$ rays is influenced by the extinction arising from the inclusions, enabling the retrieval of the inclusion concentration and size. Recently, the feasibility of rainbow refractometry for estimating the inclusion concentration of colloidal droplets by employing single wavelength extinction of intensity ratio has been demonstrated [12,35].

In the following section, the measurement principle of DERR is introduced. Section 3 then describes the experimental set-up comprising the monodisperse droplet generation system and the optical configuration of DERR. Finally, measurement results and measurement limits are presented with a comparison to analytic results in Section 4.

2. Measurement principle

Assuming the colloidal droplet can be regarded as a dilute system, the intensity attenuation of the $p = 2$ rays can be described by the Beer-Lambert law [10]:

$$I_{p=2}/I_{p=2,C_V=0} = \exp(-\mu_{ext}L), \tag{1}$$

where $I_{p=2}$ and $I_{p=2,C_V=0}$ are respectively the primary peak intensity of $p = 2$ rays through the droplet with and without the dispersed phase; C_V denotes the volume concentration of the inclusion relative to the host droplet; μ_{ext} is the volume extinction coefficient (m^{-1}). As shown in Fig. 1, L is the path length of the $p = 2$ rays traveling through the droplet and its value near the geometric rainbow angle (subscript rg) is

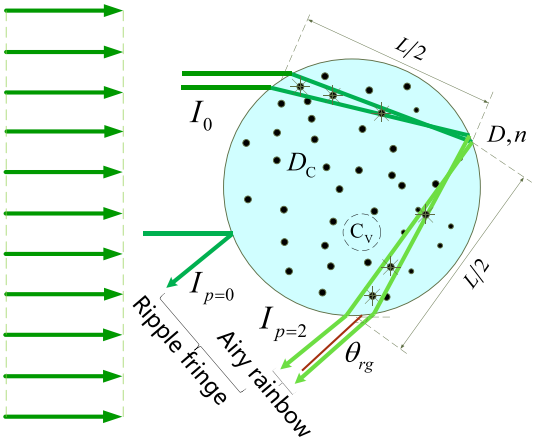

Fig. 1. Paths of $p = 2$ and $p = 0$ rays near the geometric rainbow angle within a colloidal droplet.

$$L_{rg} = 4D\sqrt{(n^2-1)/(3n^2)}, \tag{2}$$

where n and D are the refractive index and diameter of the host droplet. Both of these quantities can be known from the position and frequency of the fringes in the rainbow pattern. This formulation assumes that the beam size of the incident light is much larger than the droplet diameter and naturally much larger than the inclusion size, typically allowing measurement of particles in the size range of tens of nanometers to tens of microns.

In previous work, a method of estimating the scattering order intensity ratio $R = I_{p=2}/I_{p=0}$ has been introduced to eliminate the random fluctuations in the absolute intensity of the $p = 2$ rays [12]. These fluctuations arise from random obscuration events when the illuminating beam and/or scattered light is partially blocked by other droplets, e.g. in a spray, or when a strongly fluctuating number of droplets are recorded in the chosen exposure time. This method of estimating the intensity ratio is given in Eq. (3).

$$I_{p=2}/I_{p=2,C_V=0} = \left(\frac{I_{p=2}}{I_{p=0}}\right)/\left(\frac{I_{p=2,C_V=0}}{I_{p=0}}\right) = R/R_{C_V=0}, \tag{3}$$

where $I_{p=0}$ is the primary peak intensity of $p = 0$ rays. At low concentrations of inclusions, whether the droplet contains particles or not is assumed to have no significant effect on the magnitude of $I_{p=0}$. Therefore, the term $I_{p=2}/I_{p=2,C_V=0}$ is transformed to the attenuation of the scattering order ratio $R/R_{C_V=0}$.

The low frequency Airy rainbow and high frequency ripple fringes of the standard rainbow signal, decomposed and extracted by fast Fourier transform and inverse transform, respectively contain the amplitude information of the $p = 2$ and $p = 0$ rays. The intensity ratio $R = I_{p=2}/I_{p=0}$ can be calculated from their maximum oscillation amplitudes, expressed as

$$R = \frac{I_{p=2}}{I_{p=0}} = 16\left(\frac{A_{airy}}{A_{ripple}}\right)^2, \tag{4}$$

where A_{airy} and A_{ripple} are the maximum amplitudes of the Airy rainbow and ripple fringes respectively.

To estimate the concentration and size of the inclusion particles, it is necessary to further extract information contained in the volume extinction coefficient μ_{ext}. For droplets containing monodisperse particles,

μ_{ext} is directly related to the volume concentration C_V and the size D_c of the inclusions, expressed as

$$\mu_{ext,m} = NC_{ext} = \frac{1}{4}N\pi {D_c}^2 Q_{ext} = \frac{1.5C_V}{D_c}Q_{ext}(D_c, n_c, \lambda), \quad (5)$$

where N denotes the inclusion number concentration, C_{ext} is the inclusion extinction cross-section, and Q_{ext} is the inclusion extinction factor (a function of the incident wavelength λ, relative refractive index n_c of the inclusion to the host droplet, and diameter D_c). Similarly, the volume extinction coefficient $\mu_{ext,p}$ of the polydisperse inclusions is expressed as

$$\mu_{ext,p} = \frac{\pi}{4}\int N(D_c){D_c}^2 Q_{ext}(D_c, n_c, \lambda)\mathrm{d}D_c. \quad (6)$$

The volume concentration C_V, Sauter mean diameter D_{32} and surface area averaged extinction factor $Q_{ext,averaged}$ of the polydisperse inclusions are given by

$$C_V = \frac{\pi}{6}\int N(D_c){D_c}^3 \mathrm{d}D_c, \quad (7)$$

$$D_{32} = \frac{\int N(D_c){D_c}^3 \mathrm{d}D_c}{\int N(D_c){D_c}^2 \mathrm{d}D_c}, \quad (8)$$

$$Q_{ext,averaged} = \frac{\int N(D_c){D_c}^2 Q_{ext}(D_c, n_c, \lambda)\mathrm{d}D_c}{\int N(D_c){D_c}^2 \mathrm{d}D_c}. \quad (9)$$

Based on the Eqs. (7) to (9), Eq. (6) can be converted into

$$\mu_{ext,p} = 1.5\frac{C_V}{D_{32}}Q_{ext,averaged} \approx 1.5\frac{C_V}{D_{32}}Q_{ext}(D_{32}, n_c, \lambda). \quad (10)$$

When the dimensionless size of the inclusions $x = \pi D_c/\lambda$ is less than 4.0 (D_c<677 nm @ λ = 532 nm, 655 nm), Walters et al. [36] showed that the averaged extinction factor $Q_{ext,averaged}$ is approximately equal to $Q_{ext}(D_{32}, n_c, \lambda)$ calculated by the Lorenz-Mie theory. Thus $\mu_{ext,p}$ can still be expressed as a function of the D_{32} and C_V of the inclusions.

Referring to Eq. (1), the volume extinction coefficient μ_{ext} can be obtained from the measurement of signal intensity attenuation $I_{p=2}/I_{p=2,C_V=0}$, droplet diameter D and refractive index n of the host droplet. When the D_{32} or C_V of the inclusions is known in advance, the other parameter can be solved directly.

When both the D_{32} and C_V of the inclusions are unknowns in Eq. (10), the equation cannot be solved. By using an incident light source with two different wavelengths (λ_1 and λ_2) to simultaneously measure the same colloidal droplet, another corresponding equation can be added to jointly solve for the two parameters. This approach is called the dual-wavelength approach. The ratio $\mu_{ext,\lambda_1}/\mu_{ext,\lambda_2}$ of the extinction coefficients at the two wavelengths eliminates C_V, and is expressed as

$$\mu_{ext,\lambda_1}\mu_{ext,\lambda_2} = \frac{Q_{ext}(D_c, n(\lambda_1), \lambda_1)}{Q_{ext}(D_c, n(\lambda_2), \lambda_2)}. \quad (11)$$

As shown in Fig. 2, the extinction factor ratio $Q_{ext,655nm}/Q_{ext,532nm}$ at the two wavelengths oscillates with particle size D_c, which results in multiple ambiguous solutions for the same extinction factor ratio. However, a unique solution can be determined when the approximate range of D_c is known *a prior* and then the dual-wavelength approach is again feasible. The figure demonstrates a measurable non-ambiguous size range of 0–2.0 μm, and the inclusion size in this study is a few hundred nanometers, which fits the present applicable range. It is worth noting that this extinction ratio based method for measuring the D_c and C_V of inclusions is only applicable to isotropic and spherical particles, as is also a requirement for for the host droplet.

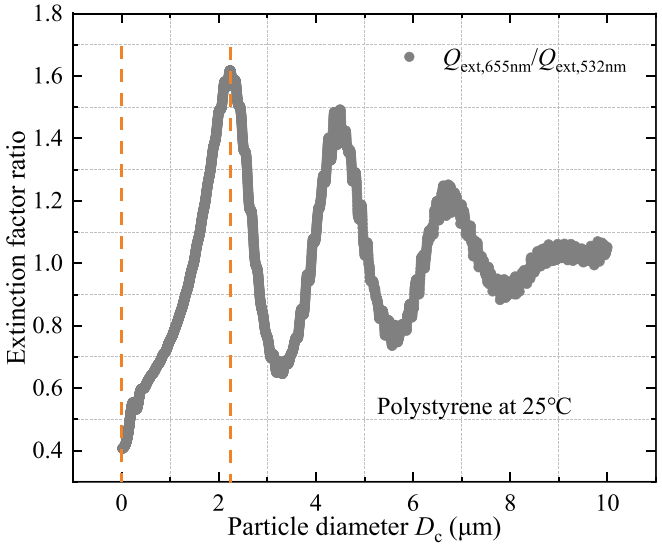

Fig. 2. Extinction factor ratio ($Q_{ext,655nm}/Q_{ext,532nm}$) of polystyrene versus particle diameter.

3. Experimental setup

The monodisperse droplet generation system and dual-wavelength rainbow measurement are depicted in Fig. 3. The inclusions in the experiments were polystyrene (PS) particles and the host droplet is deionized water. By means of precisely controlled dilution, the monodisperse PS particles (C_V = 10%) with diameters of 210 (±3) nm or 530 (±5) nm are dispersed into the deionized water using a microelectronic balance, yielding suspensions with different volume concentrations (C_V = 0%, 0.1%, 0.2% and 0.3%). As shown in Fig. 4, the PS particles were examined using SEM, yielding an average size, used later for comparison to the size measured using DERR. The sphericity and size monodispersity of the particles are evidently very good.

Nanoparticles in suspensions are highly susceptible to agglomeration under the combined effect of van der Waals forces, gravitational forces and electrostatic repulsions. The probability of agglomeration is related to the frequency of collisions between particles and is directly affected by particle concentration. On the one hand, the particle concentrations studied in this investigation are relatively low. On the other hand, ultrasonic oscillation can effectively reduce the agglomeration of nanoparticles and make them fully dispersed. Therefore, the suspensions were placed in an ultrasonic oscillator (model F-008S, 0.8 L, power 80 W) for 15 min before transferring to the syringe pump. Moreover, the density of PS particles is almost the same as that of water, diminishing the settling of PS particles due to gravity [35,37].

The monodisperse droplet generation system comprises a monodisperse droplet generator (vibrating orifice), a high-pressure syringe pump, a signal generator, and a three-dimensional displacement device. The suspension was injected into a monodisperse droplet generator (MTG-01-G1, FMP) at a flow rate of Q = 2.0 ml/min by a high precision, high pressure syringe pump (LSP01-1BH, ±0.5%). A capillary jet was formed through the nozzle orifice with a diameter of 100 μm. Under a periodic disturbance (f = 14.5 kHz) imposed by a piezoelectric ceramic driven by the signal generator (TOE 7404), the jet undergoes a Rayleigh-Plateau instability and breaks up into equally spaced droplets with known diameter. It is noteworthy that the monodisperse droplet generation system is able to produce stable, uniform colloidal droplets due to the low concentration of the added inclusions.

Two vertically polarized (polarization ratio >100) laser beams emitted from two lasers with wavelengths of 655 nm and 532 nm (Model: MSII-N-655-200mW, MSII-N-532-200mW) were merged into a single

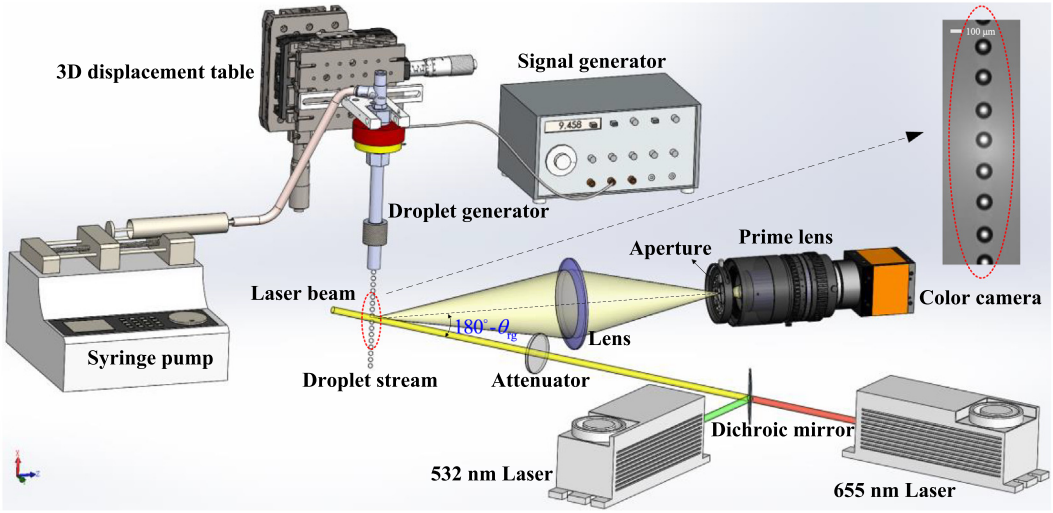

Fig. 3. Schematic of experimental setup.

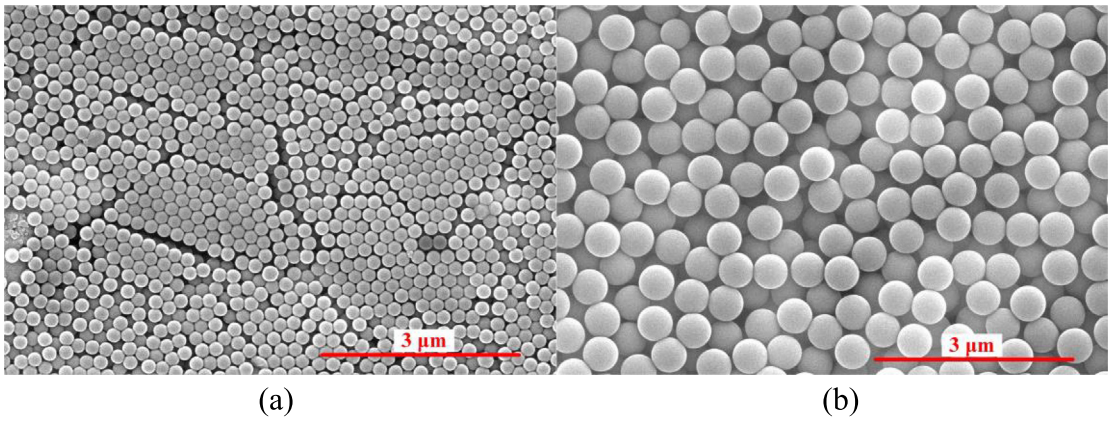

Fig. 4. SEM images of studied monodisperse polystyrene particles: (a) 210 nm and (b) 530 nm using a magnification factor of 5×10^4.

beam through a dichroic mirror (DMLP567R). After passing through the attenuator, the merged laser beam illuminated the colloidal droplets to be measured. The generated dual-wavelength extinction rainbow signal was collected and recorded by an imaging system consisting of an aspherical lens (focal length = 150 mm, diameter = 75 mm), an aperture (size = 1 mm), a prime lens (MV2514-5M), and a color camera (Basler acA1920-40gc). In this experiment, the exposure time of the camera was set to 0.2 ms and the number of droplets recorded in a single frame image was 2–4, avoiding the distortion of the ripple fringes due to minute droplet diameter variations between droplets.

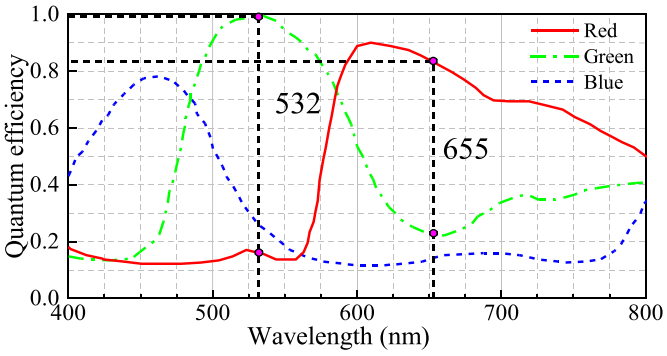

Fig. 5. Spectral response curve of the color camera.

The color camera records the image of RGB three channels, which contains the rainbow signals at the two wavelengths. However, the red (R) and green (G) channels both respond to these two wavelengths. According to the spectral response characteristics of the camera sensor chip as illustrated in Fig. 5, the signal intensities corresponding to wavelengths $\lambda_1 = 655$ nm (I_{λ_1}) and $\lambda_2 = 532$ nm (I_{λ_2}) can be separated from the R and G channels as follows,

$$I_{\lambda_1} = \frac{I_{\text{camera,R}}/R_{\lambda_2} - I_{\text{camera,G}}/G_{\lambda_2}}{R_{\lambda_1}/R_{\lambda_2} - G_{\lambda_1}/G_{\lambda_2}},$$
$$I_{\lambda_2} = \frac{I_{\text{camera,R}}/R_{\lambda_1} - I_{\text{camera,G}}/G_{\lambda_1}}{R_{\lambda_2}/R_{\lambda_1} - G_{\lambda_2}/G_{\lambda_1}} \quad (12)$$

where the coefficients $R_{\lambda_1} = 0.826$, $R_{\lambda_2} = 0.226$, $G_{\lambda_1} = 0.139$, $G_{\lambda_2} = 0.994$ are the wavelength dependent response quantum efficiencies of the R and G channels. $I_{\text{camera,R}}$ and $I_{\text{camera,G}}$ are the intensity of R and G channels recorded by the camera.

Each pixel in the recorded color image is processed using Eq. (12), which can separate the dual-wavelength rainbow signals according to

their respective wavelengths, as shown in Fig. 6. The Airy rainbow and ripple fringes are very clear in both separated images. The 532 nm rainbow image is brighter than the 655 nm one due to the stronger response of the camera to the 532 nm green light.

4. Results and analysis

4.1. Rainbow pattern with dual-wavelength extinction configuration

Since an analytical/numerical approach to compute the light scattered from micron sized colloidal droplets is not available or practical, a Monte Carlo based ray tracing procedure [38] was used to simulate some features of the rainbow signals obtained in the experiment. The ray tracing routine used did not preserve the phase or polarization of the rays; hence, interference phenomena could not be captured. Nevertheless, the intensity of the primary Airy peak is obtained, which still contributes to an understanding of the extinction characteristics within the colloidal droplets and can provide a reference for experimental studies.

Fig. 7 illustrates the simulated light scattering intensity distributions of colloidal droplets ($D = 164\ \mu$m) at different inclusion concentrations ($C_V = 0\%, 0.1\%, 0.2\%, 0.3\%$) and sizes ($D_c = 210$ nm, 530 nm) using a laser illumination at $\lambda = 655$ nm and $\lambda = 532$ nm. The insert in each figure magnifies the angular scale near the geometric rainbow angle, and it can be clearly seen that the intensity of the rainbow primary peak decreases with inclusion concentration and size. Furthermore, the peak attenuation at $\lambda = 532$ nm is stronger than that at $\lambda = 655$ nm.

Dual-wavelength rainbow images of colloidal droplets of different inclusion concentrations and sizes obtained experimentally at an ambient temperature of 25 C are illustrated in Fig. 8. Compared to the rainbow pattern obtained for pure water ($C_V = 0\%$), the rainbow images of colloidal droplets exhibit a uniform background intensity. Light, originally contributing to the rainbow primary peak, is scattered by inclusions and is redirected to nearby angular positions, forming the observed background. Its intensity, representing the extinction degree, increases with the inclusion concentration and size. In addition, the background appears green because of the stronger extinction of the $\lambda = 532$ nm light to the experimental inclusions. Therefore, when the background is omitted, the signal from $\lambda = 655$ nm gradually occupies more intensity proportion of the original rainbow signal with the increase of C_V. The rainbow image becomes redder with increasing inclusion concentration, which is especially obvious in the case of $C_V = 0.3\%$.

Using the same image analysis procedure as was used for Fig. 6, each image in Fig. 8 was first separated into 532 nm and 655 nm rainbow images. The intensity for each horizontal pixel position was averaged over 100 rows of pixels around the mid-height of the separated rainbow images. The scattering angle results were combined to plot the normalized intensity distribution as a function of angular position, as shown in Fig. 9. To visualize rainbow signals at different nanoparticle volume concentrations more clearly, the four curves have been plotted on shifted x-axis scales. The features of the dual-wavelength extinction rainbow signal in Fig. 9 are as follows: (I) With an increase of inclusion concentration, the modulation depth of the ripple fringes relative to the Airy rainbow is enhanced (signal of $\lambda = 532$ nm exhibits more modulation). This is due to the attenuation of $p = 2$ rays inside the drop which contribute to the Airy main peak. (II) The background due to internal scattering of inclusions is most clearly reflected in the leftmost part of the rainbow primary peak, also called Alexander's dark band, and its intensity increases with C_V (almost zero when $C_V = 0\%$). (III) The extinction effect decreases with λ and increases with D_c, which is consistent with the simulated results in Fig. 7. (IV) The primary peak scattering angle of the rainbow signal of $\lambda = 532$ nm is slightly larger than that of $\lambda = 655$ nm at the same C_V, which is attributed to the larger relative refractive index at $\lambda = 532$ nm than at $\lambda = 655$ nm.

4.2. Estimation of parameters

Estimation of the various desired parameters from the rainbow signals is achieved iteratively by minimizing the least squares deviation between experimental and computed rainbow signals using the modified Nussenzveig theory [39]. The obtained parameter values are then averaged over signals from 60 droplets, all generated under the same conditions. Fig. 10 presents the measured refractive index, droplet diameter and their errors obtained with different excitation frequencies

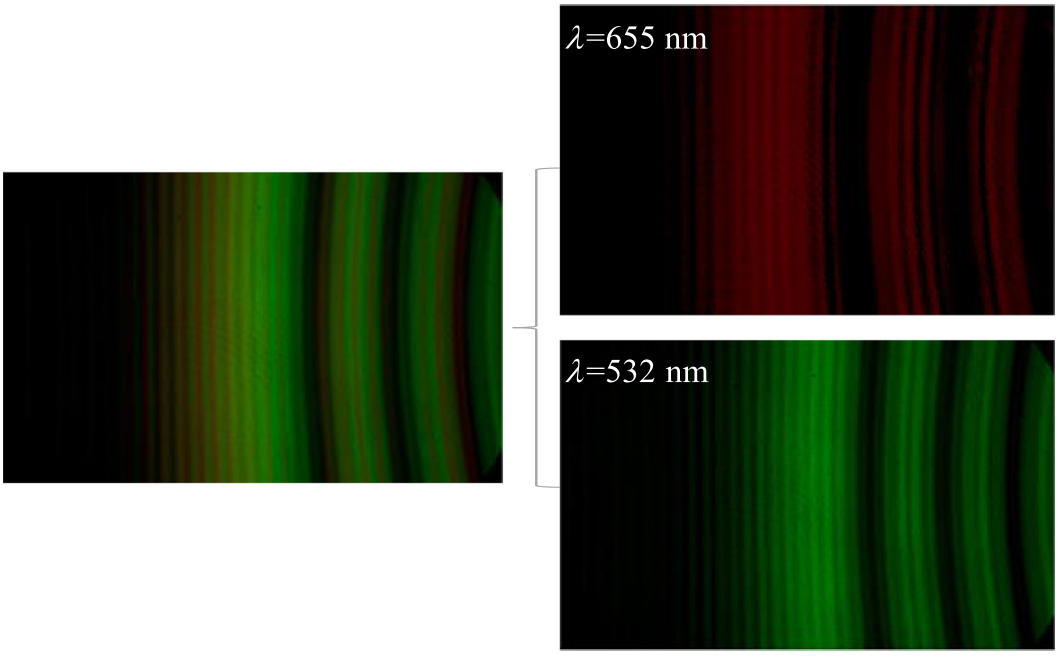

Fig. 6. Dual-wavelength rainbow image is separated into red (655 nm) and green (532 nm) rainbow images.

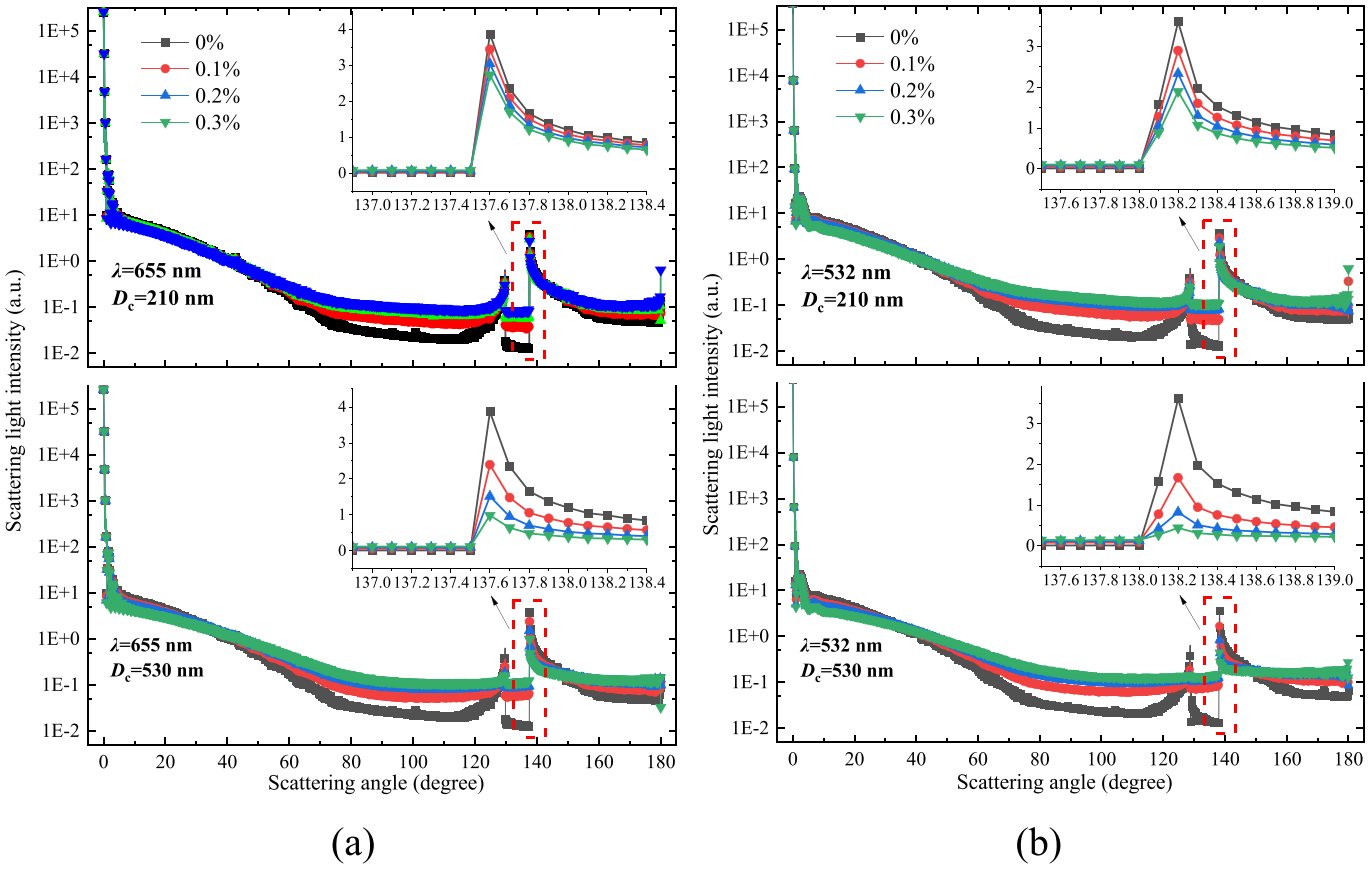

Fig. 7. Simulated light scattering intensity distributions of colloidal droplets ($D = 164\,\mu$m) at different inclusion concentrations (C_V = 0%, 0.1%, 0.2%, 0.3%) and sizes (D_c = 210 nm, 530 nm): (a) λ = 655 nm, (b) λ = 532 nm.

of the droplet generator, i.e. for different droplet diameters. Results are shown for values obtained for each of the two wavelengths.

As the droplet generator frequency increases, the measured refractive index of the host droplet (liquid phase) remains constant and the measured droplet diameter decreases, as expected. The droplet diameters measured at the two wavelengths agree very well with one another, confirming the accuracy of the measurement. The true value of the refractive index in Fig. 10(a) is computed using an empirical formula related to temperature and wavelength [40], and according to this estimation, the maximum error in measured refractive index is about 4×10^{-4}. Since the path length L is very insensitive to the refractive index n, this input into the estimation of n only accounts for an error of less than 0.04% and can be neglected. The true value of droplet diameter, shown by the dashed line in Fig. 10(b), is predicted by the well-known Rayleigh-Plateua jet breakup formula [41]. The measured values match these predicted values very well, with an average relative error below 1%.

The next set of measurement results were obtained for the fixed frequency of f = 14.5 kHz of the droplet generator. At this frequency the measured droplet diameter given in Fig. 10 was 164.2 μm. The measured refractive indices of the droplet at λ = 655 nm and λ = 532 nm were respectively 1.3305 and 1.3344. The path lengths L_{rg} at the

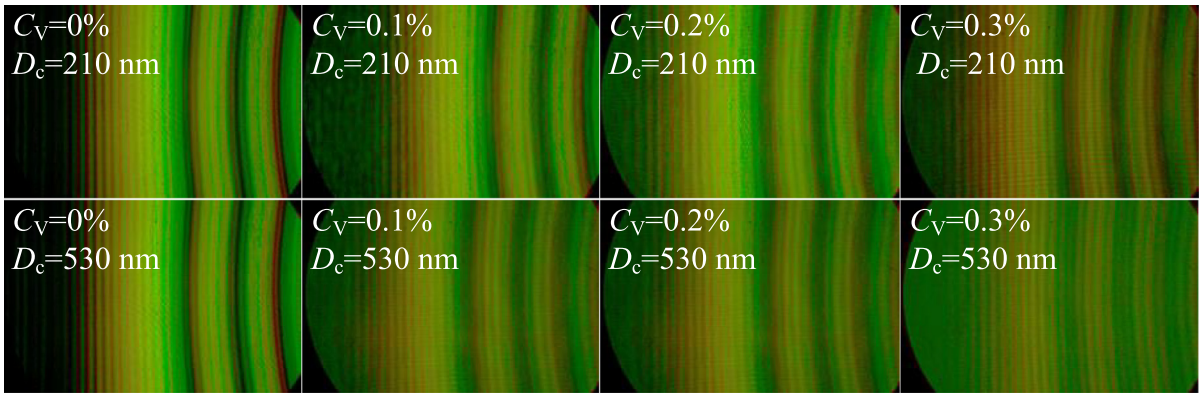

Fig. 8. Recorded typical dual-wavelength rainbow images of colloidal droplets of different inclusion concentrations and sizes.

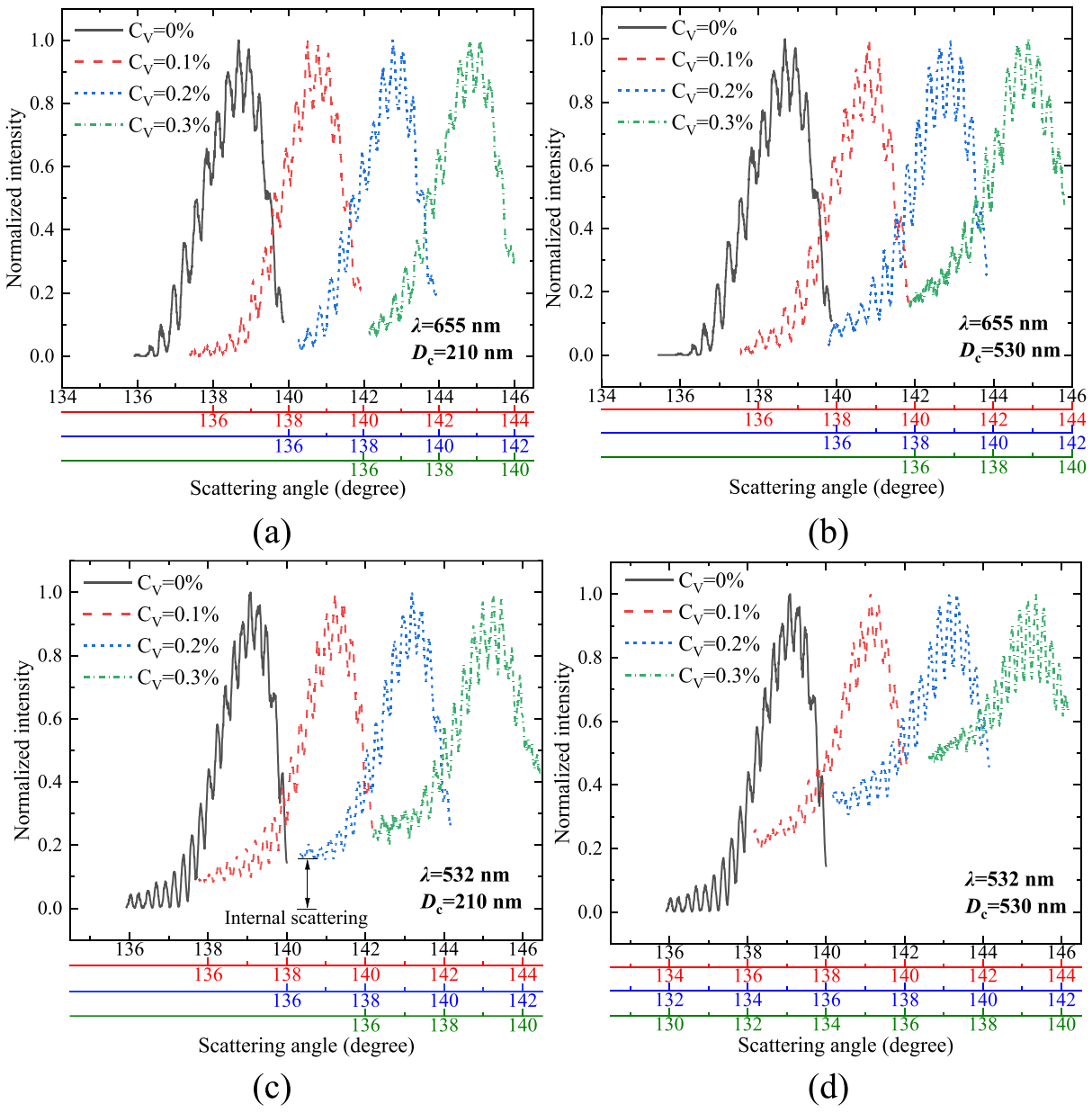

Fig. 9. Experimental dual-wavelength normalized rainbow signals extracted from images in Fig. 8: (a) λ = 655 nm, D_c = 210 nm, (b) λ = 655 nm, D_c = 530 nm, (c) λ = 532 nm, D_c = 210 nm, and (d) λ = 532 nm, D_c = 530 nm.

two wavelengths are calculated to be 250.16 μm and 251.08 μm respectively.

The amplitudes of the Airy rainbow peaks and ripple fringes of the extinction rainbow signals are first extracted and the scattering order intensity ratios R are calculated according to Eq. (4). Fig. 11 presents the measured attenuation ratios of the R at different inclusion concentrations C_V, and the dashed lines are the predictions using Eq. (1). The measured and predicted values agree reasonably well. As expected, the attenuation ratio increases with C_V and the slope of its growth decreases. This decreasing growth rate is most obvious at the operating condition of D_c = 530 nm, because the extinction factor Q_{ext} at λ = 530 nm of PS particles is much larger than that at 210 nm. In addition, an increase in the illuminating wavelength leads to a decrease in the attenuation ratio, which is consistent with the simulated results described in Section 4.1.

Based on the measured attenuation ratios of the R and the host droplet parameters (droplet diameter and refractive index), the volume extinction coefficients μ_{ext} at the two wavelengths and their ratios $\mu_{ext,655nm}/\mu_{ext,532nm}$ are calculated based on Eqs. (1) and (11). The inclusion particle sizes D_c are then estimated based on the monotonic relationship (shown in Fig. 2) between the extinction factor ratio and the inclusion size. Finally, the values of D_c are substituted into Eq. (10) to determine C_V. Table 1 presents the measured values of μ_{ext} and their ratios at the two wavelengths.

Fig. 12 summarizes the measured inclusion particle size D_c, volume concentration C_V and their errors. As shown in Fig. 12(a), the measured inclusion particles sizes are respectively 193 nm, 192 nm and 187 nm at the operating conditions where D_c = 210 nm and C_V = 0.1%, 0.2%, 0.3%, with absolute and relative errors of −17 nm (−8.1%), −18 nm (−8.6%) and −23 nm (−11.0%). At the operating conditions of D_c = 530 nm, the measured values are 543 nm, 510 nm and 585 nm, corresponding to errors of 13 nm (2.5%), −20 nm (−3.8%) and 55 nm (10.4%), respectively. Fig. 12(b) shows that the measured volume concentrations at D_c = 210 nm are 0.105%, 0.222%, and 0.347% respectively, and the corresponding

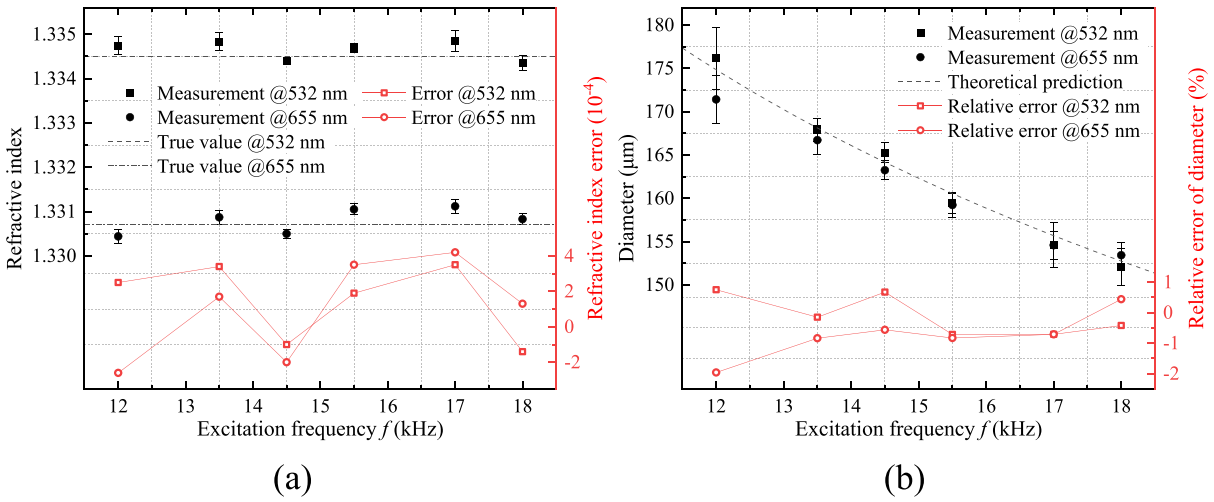

Fig. 10. Measured values and errors of (a) refractive index and (b) droplet diameter of the host droplet with different droplet generator excitation frequencies for the wavelengths 655 nm and 532 nm.

absolute and relative errors are 0.005% (5.0%), 0.022% (11.0%), and 0.047% (15.7%). At $D_c = 530$ nm, the volume concentrations of inclusions measured are 0.094%, 0.192% and 0.246%, corresponding to the errors of −0.006% (−6.0%), −0.008% (−4.0%) and −0.054% (−18.0%) respectively. The measurement accuracy of inclusion size is slightly higher than that of volume concentration at both operating conditions. This is mainly due to the fact that the particle size is determined first during the estimation, and the error in size propagates further to the estimation of volume concentration. The measurement error of both parameters (C_V and D_c) increases with increasing volume concentration. At relatively low concentrations ($C_V = 0.1\%, 0.2\%$), the measurement errors of C_V are small and do not exceed 11.0%, which is an acceptable error. However, the measurement errors at relatively high concentration ($C_V = 0.3\%$) increase significantly (up to 18.0%), which is still an acceptable error for engineering applications. This is because the slope (i.e. sensitivity) of the signal attenuation ratio to the volume concentration (growth rate) decreases with increasing volume concentration, as depicted in Fig. 11. Thus, with the same absolute error of the measured attenuation ratio, the corresponding absolute error of the volume concentration increases with C_V.

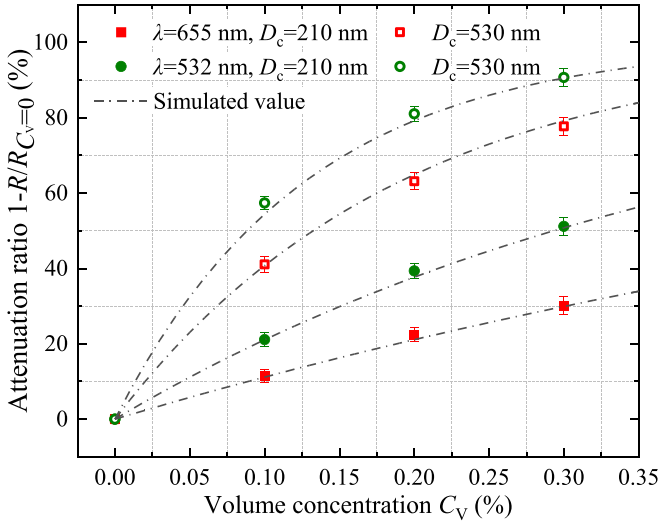

Fig. 11. Measured attenuation ratios of the scattering order intensity ratio R versus the inclusion concentration.

By substituting the exact values of inclusion particle size D_c or volume concentration C_V and the measured value of extinction coefficient shown in Table 1 into Eq. (10), the measured values and errors of the other parameter are calculated, as depicted in Fig. 13. The measurement errors of the D_c shown in Fig. 13(a) are overall comparable to the errors in Fig. 12(a) when C_V is known. On the contrary, when inclusion particle size is known *a prior*, the measurement errors of C_V shown in Fig. 13 (b) are smaller than the error in Fig. 12(b). This verifies the conclusion that the measurement error of C_V in Fig. 12(b) is partly caused by the propagation of the size measurement error. When the measurement of C_V is of more interest, the D_c should be known in advance to obtain more accurate values of C_V. Furthermore, it is evident that the measured values at $\lambda = 532$ nm are more accurate than those at $\lambda = 655$ nm when $D_c = 210$ nm, but for $D_c = 530$ nm the two are almost identical. This is understandable, since when the extinction effect (factor) of the inclusions is small, namely a small attenuation, then the measurement error caused by the signal extraction accounts for a larger proportion. To measure colloidal droplets with a high inclusion concentration, the incident wavelength needs to be selected such that the extinction effect of the inclusions at this wavelength is as small as possible; for the measurement of colloidal droplets with low inclusion concentration, the incident wavelength should be higher.

4.3. Measurement limits

Assuming that the inclusion particles are not agglomerated, the measurable range of C_V is determined by multiple factors, such as the measurable extinction ratio of the $p = 2$ rays, the properties of the host droplet and inclusion particles, as expressed in Eq. (10). The experimentally obtainable extinction ratio (i.e. attenuation ratio $I_{p=2}/I_{p=2,C_V=0}$) of the rainbow primary peak, is considered to be about

Table 1
Measured values of the volume extinction coefficient μ_{ext} at two wavelengths and their ratios.

D_c (nm)	CV	$\mu_{ext,532nm}$ (m^{-1})	$\mu_{ext,655nm}$ (m^{-1})	Ratio
210	0.1%	957.6	499.4	0.521
	0.2%	2026.4	1055.3	0.520
	0.3%	2999.9	1541.2	0.513
530	0.1%	3393.3	2112.0	0.622
	0.2%	6524.1	3989.1	0.611
	0.3%	9451.9	5994.5	0.634

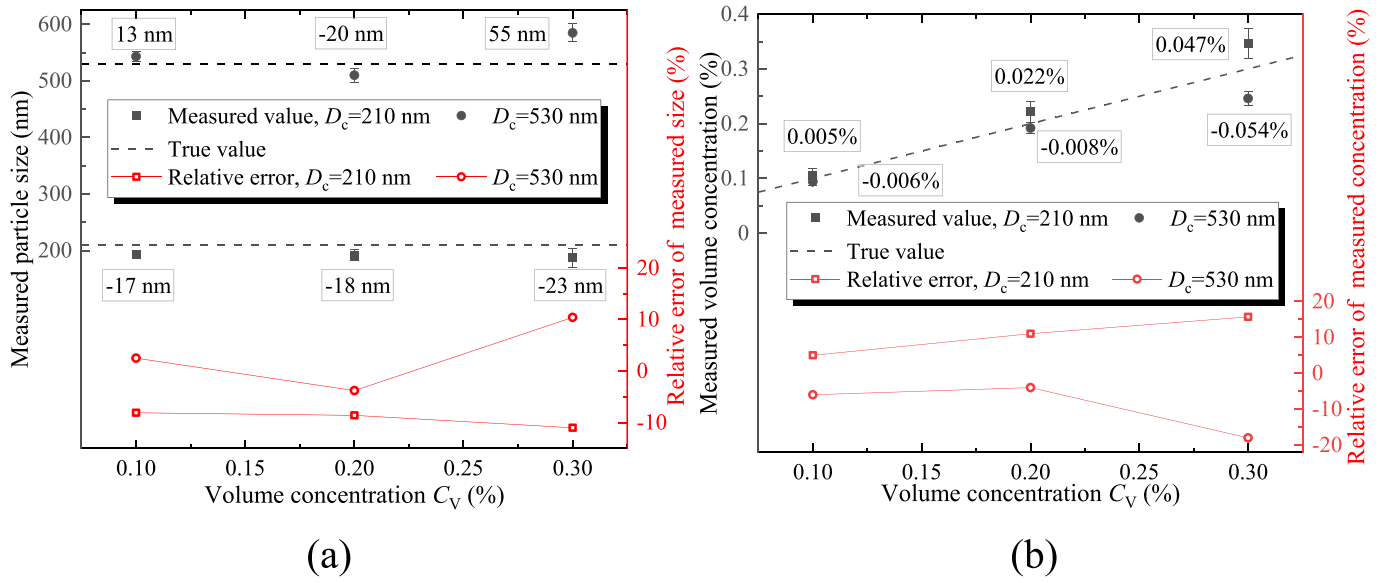

Fig. 12. Measured values and errors of (a) inclusion particle size and (b) volume concentration.

5–90%. When the attenuation ratio is less than 5%, it is difficult to distinguish the signal attenuation from the signal noise. When it is greater than 90%, the model of light scattered by the inclusions is multiple scattering. The suspension cannot be regarded as a dilute system and the condition of Eq. (1) is thus no longer satisfied.

Taking the dual-wavelength light source, deionized water, and inclusion particles from this study as examples, the measurable range of C_V, varying with the D_c under different host droplet diameters ($D = 30, 100, 200\ \mu m$), is calculated and shown in Fig. 14. The upper and lower limits of the measurable C_V both decrease with increasing D and the D_c. Especially when D_c is less than 200 nm, the decrease is even exponential. Since the extinction level of our tested inclusion particles is high, the investigated number concentration in our experiment is relatively low. However, the DERR can measure higher solid holdup levels (up to tens of percent), if the size of inclusion particles and the host droplet are reduced to tens of nanometers and micrometers respectively, as shown in Fig. 14. In fact, the upper limit of C_V is simultaneously affected by particle agglomeration, which remains to be studied, and of course less than the value shown in Fig. 14. Since the inclusions are more likely to be polydispersed, based on the applicable conditions of Eq. (10) and the minimum measurable concentration is not higher than 100%, the measurable range of the D_c is roughly estimated to be 22–677 nm. Taking into account that the ripples must be distinguished from the Airy rainbow pattern, and demanding a certain minimum signal-to-noise ratio, the minimum droplet diameter that can be measured is estimated to be about 30 μm. Large droplets will become non-spherical more readily and the maximum measurable droplet diameter will be limited, since sphericity is a fundamental prerequisite of dual wavelength rainbow refractometry. Thus a conservative estimate of the largest measurable droplet diameter is 200 μm.

In the implementation and application of DERR, two further limiting factors should be noted. One is the above-mentioned measureable

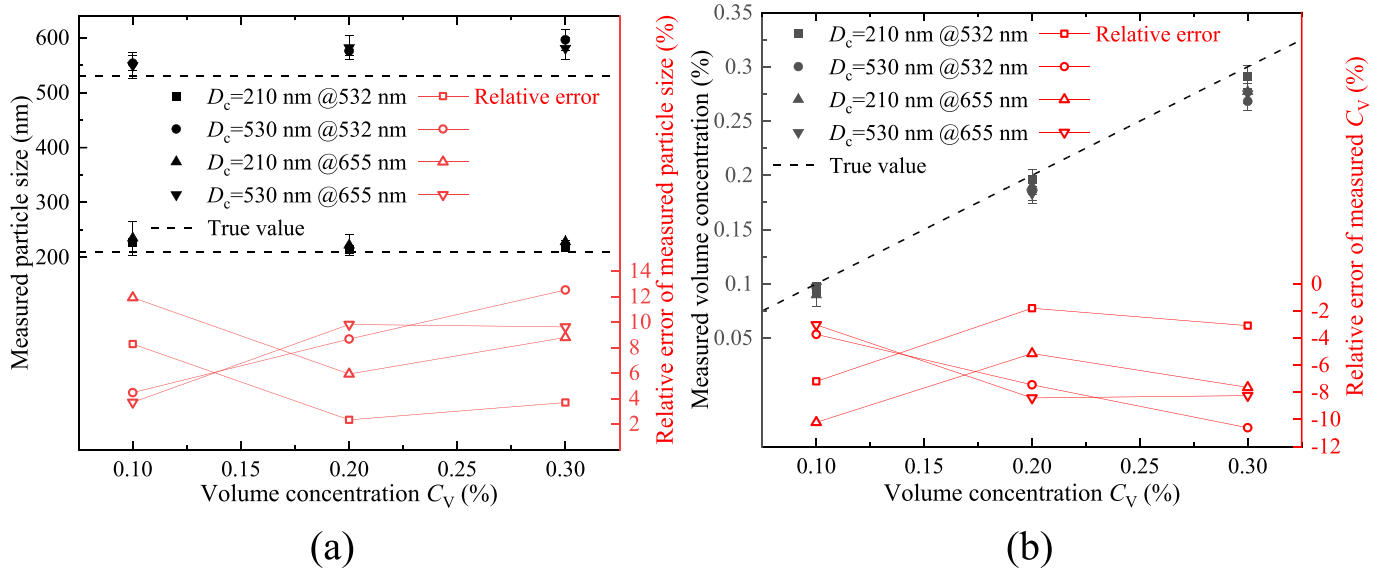

Fig. 13. Provided that (a) volume concentration or (b) size of the inclusions is known, the measured value of the other parameter and its error.

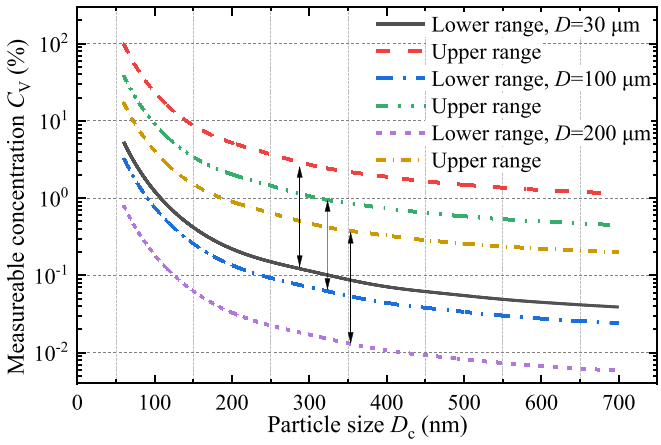

Fig. 14. Measurable volume concentration range varies with the inclusion size under different host droplet diameters of $D = 30 thinmathspace \mu$m, 100 μm, and 200 μm.

concentration range, since at higher concentrations agglomeration of the inclusion particles may become significant. Another issue is the non-spherical droplets, arising from a multitude of sources: droplet/droplet collisions, droplet oscillations just after the atomization process, partial drying of droplets in spray drying scenarios. As rainbow refractometry is sensitive to the droplet shape, non-spherical droplets exhibit irregular rainbow patterns which can be recognized during the post processing and rejected from further analysis. However, the direct measurement of non-spherical droplets is currently beyond the scope of the present study.

5. Summary and concluding remarks

Dual-wavelength extinction rainbow refractometry (DERR) has been proposed to optically characterize colloidal droplets. Under combined dual-wavelength ($\lambda = 532$ nm, 655 nm) light illumination, validation experiments using deionized water droplets containing standard polystyrene nanoparticles with different volume concentrations ($C_V = 0\%$, 0.1%, 0.2%, 0.3%) and particle sizes ($D_c = 210$ nm, 530 nm) were conducted. Important conclusions are summarized below.

- A background intensity, caused by the internal scattering of the inclusions, overlays the measured rainbow patterns. Its intensity, most clearly seen in the angular region of Alexander's dark band, increases with C_V (almost zero when $C_V = 0\%$).
- The droplet diameters measured at $\lambda = 532$ nm, 655 nm are very close to one another and agree well with theoretical values. The maximum measurement error of refractive index is about 4×10^{-4}. The C_V and D_c of the inclusions can be simultaneously estimated. In the case of $D_c = 210$ nm, the maximum absolute and relative errors of D_c are −23 nm (−11.0%), and that of C_V are 0.047% (15.7%). For $D_c = 530$ nm, the maximum errors of D_c are 55 nm (10.4%), and that of C_V are −0.054% (−18.0%). The above measurement results confirm the feasibility and accuracy of DERR. The errors of C_V and D_c, both increase with C_V. At relatively low concentrations ($C_V = 0.1\%, 0.2\%$), the errors of C_V are small (no more than 11.0%); but the error at relatively high concentration ($C_V = 0.3\%$) increases significantly (up to 18.0%). This is because the sensitivity of the signal attenuation ratio to C_V decreases with C_V.
- When C_V is known *a prior*, the error for D_c is comparable to that in cases with two unknown parameters. However, when D_c is known, the error of C_V is smaller. The measured values at $\lambda = 532$ nm are more accurate than those at $\lambda = 655$ nm when $D_c = 210$ nm, but for $D_c = 530$ nm the two are almost identical, which is because the error caused by the signal extraction dominates the overall measurement error when the extinction of the inclusions is relatively weak.
- Assuming that the inclusion particles do not agglomerate, the upper and lower limits of the measurable C_V, jointly determined by the measurable extinction ratio of the signal, the properties of host droplet and inclusion, both decrease with increasing D and D_c. When the D_c is less than 200 nm, the decrease is even exponential. The measurable range of D_c is roughly estimated as 22–677 nm, and that of D is 30–200 μm.

The present simultaneous measurement of inclusion concentration and size relies on the approximate range of inclusion size, which can be circumvented by a light source with three different wavelengths being considered in future work. The agglomeration of nanoparticles tends to be more severe as the size decreases, and one possible way to overcome this is to add surfactants. However, the measurement limits of colloidal droplets with inclusion size less than 100 nm and the effect of the surfactants remain to be investigated. Compared with the traditional extinction method, the most notable advantage of DERR is its online measurement capability, facilitating future applications in the *in-situ* characterization of suspension sprays.

Declaration of Competing Interest

The authors declare that they have no known competing financial interests or personal relationships that could have appeared to influence the work reported in this paper.

Acknowledgements

The authors gratefully acknowledge the support from project supported by National Natural Science Foundation of China (52006193), Natural Science Foundation of Jiangsu Province (BK20190439), and Shuangchuang Program of Jiangsu Province (JSSCBS20210207).

References

[1] M.E.M. Soudagar, N.-N. Nik-Ghazali, M.A. Kalam, I. Badruddin, N. Banapurmath, N. Akram, The effect of nano-additives in diesel–biodiesel fuel blends: a comprehensive review on stability, engine performance and emission characteristics, Energy Convers. Manage. 178 (2018) 146–177.
[2] R. de Souza Lima, M.-I. Ré, P. Arlabosse, Drying droplet as a template for solid formation: a review, Powder Technol. 359 (2020) 161–171.
[3] M. Malý, A. Moita, J. Jedelsky, A. Ribeiro, A. Moreira, Effect of nanoparticles concentration on the characteristics of nanofluid sprays for cooling applications, J. Therm. Anal. Calorim. 135 (6) (2019) 3375–3386.
[4] K.N. Al-Milaji, V. Radhakrishnan, P. Kamerkar, H. Zhao, ph-modulated self-assembly of colloidal nanoparticles in a dual-droplet inkjet printing process, J. Colloid Interface Sci. 529 (2018) 234–242.
[5] C. Tian, Y. Cai, H. Yang, M. Su, Investigation on mixed particle classification based on imaging processing with convolutional neural network, Powder Technol. 391 (2021) 267–274.
[6] H. Yang, M. Su, X. Wang, J. Gu, X. Cai, Particle sizing with improved genetic algorithm by ultrasound attenuation spectroscopy, Powder Technol. 304 (2016) 20–26.
[7] H. Lee, D.-B. Kwak, S.C. Kim, D.Y. Pui, Characterization of colloidal nanoparticles in mixtures with polydisperse and multimodal size distributions using a particle tracking analysis and electrospray-scanning mobility particle sizer, Powder Technol. 355 (2019) 18–25.
[8] T.D. Fansler, S.E. Parrish, Spray measurement technology: a review, Meas. Sci. Technol. 26 (1) (2014) 012002.
[9] Y. Han, Z. Cui, W. Zhao, Scattering of gaussian beam by arbitrarily shaped particles with multiple internal inclusions, Opt. Express 20 (2) (2012) 718–731.
[10] L. Li, Light Scattering of Complex Particles: Application to the Time-Shift Technique, Technische Universität Darmstadt, Darmstadt, 2020 Ph.D. thesis.
[11] L. Li, C. Tropea, Measurement of the colloidal particle concentration and size within a drop using the time-shift technique, J. Quant. Spectrosc. Radiat. Transfer 263 (2021) 107548.
[12] C. Li, Y. Wu, X. Wu, C. Tropea, Simultaneous measurement of refractive index, diameter and colloid concentration of a droplet using rainbow refractometry, J. Quant. Spectrosc. Radiat. Transfer 245 (2020) 106834.
[13] U.K. Krieger, C. Braun, L. Imbach, T. Koop, T. Corti, G. Videen, An experimental examination of intensity fluctuations of a host droplet containing an inclusion, J. Quant. Spectrosc. Radiat. Transfer 79 (2003) 873–880.

[14] D. Jakubczyk, G. Derkachov, M. Zientara, M. Kolwas, K. Kolwas, Local-field resonance in light scattering by a single water droplet with spherical dielectric inclusions, J. Optic. Soc. Am. A 21 (12) (2004) 2320–2323.
[15] Y. Wei, W. Deng, R.-H. Chen, Effects of insoluble nano-particles on nanofluid droplet evaporation, Int. J. Heat Mass Transfer 97 (2016) 725–734.
[16] S. Tanvir, L. Qiao, Droplet burning rate enhancement of ethanol with the addition of graphite nanoparticles: influence of radiation absorption, Combust. Flame 166 (2016) 34–44.
[17] A. Saha, S. Basu, R. Kumar, Particle image velocimetry and infrared thermography in a levitated droplet with nanosilica suspensions, Exp. Fluids 52 (3) (2012) 795–807.
[18] K. Pandey, S. Basu, How boiling happens in nanofuel droplets, Phys. Fluids 30 (10) (2018) 107103.
[19] W. Wichitwong, S. Coëtmellec, D. Lebrun, D. Allano, G. Gréhan, M. Brunel, Long exposure time digital in-line holography for the trajectography of micronic particles within a suspended millimetric droplet, Optic. Commun. 326 (2014) 160–165.
[20] T. Wriedt, R. Schuh, The inclusion-concentration measurement of suspension droplets based on Monte Carlo ray tracing, Meas. Sci. Technol. 13 (3) (2002) 276.
[21] N. Riefler, R. Schuh, T. Wriedt, Investigation of a measurement technique to estimate concentration and size of inclusions in droplets, Meas. Sci. Technol. 18 (7) (2007) 2209.
[22] L. Li, P.G. Stegmann, S. Rosenkranz, W. Schäfer, C. Tropea, Simulation of light scattering from a colloidal droplet using a polarized monte carlo method: application to the time-shift technique, Opt. Express 27 (25) (2019) 36388–36404.
[23] K. Anoop, R. Sadr, R. Yrac, M. Amani, Rheology of a colloidal suspension of carbon nanotube particles in a water-based drilling fluid, Powder Technol. 342 (2019) 585–593.
[24] S. Basu, A. Miglani, Combustion and heat transfer characteristics of nanofluid fuel droplets: a short review, Int. J. Heat Mass Transfer 96 (2016) 482–503.
[25] N. Roth, K. Anders, A. Frohn, Refractive-index measurements for the correction of particle sizing methods, Appl. Opt. 30 (33) (1991) 4960–4965.
[26] C.D. Rosebrock, S. Shirinzadeh, M. Soeken, N. Riefler, T. Wriedt, R. Drechsler, L. Mädler, Time-resolved detection of diffusion limited temperature gradients inside single isolated burning droplets using rainbow refractometry, Combust. Flame 168 (2016) 255–269.
[27] H. Yu, F. Xu, C. Tropea, Optical caustics associated with the primary rainbow of oblate droplets: simulation and application in non-sphericity measurement, Opt. Express 21 (22) (2013) 25761–25771.
[28] A. Verdier, J.M. Santiago, A. Vandel, S. Saengkaew, G. Cabot, G. Gréhan, B. Renou, Experimental study of local flame structures and fuel droplet properties of a spray jet flame, Proc. Combust. Ins. 36 (2) (2017) 2595–2602.
[29] M. Ouboukhlik, G. Godard, S. Saengkaew, M.-C. Fournier-Salaün, L. Estel, G. Gréhan, Mass transfer evolution in a reactive spray during carbon dioxide capture, Chem. Eng. Technol. 38 (7) (2015) 1154–1164.
[30] Y. Wu, C. Li, J. Cao, X. Wu, S. Saengkaew, L. Chen, G. Gréhan, K. Cen, Mixing ratio measurement in multiple sprays with global rainbow refractometry, Exp. Therm. Fluid Sci. 98 (2018) 309–316.
[31] C. Li, Q. Lv, Y. Wu, X. Wu, C. Tropea, Measurement of transient evaporation of an ethanol droplet stream with phase rainbow refractometry and high-speed microscopic shadowgraphy, Int. J. Heat Mass Transfer 146 (2020) 118843.
[32] Y. Wu, H. Li, X. Wu, G. Gréhan, L. Mädler, C. Crua, Change of evaporation rate of single monocomponent droplet with temperature using time-resolved phase rainbow refractometry, Proc. Combust. Ins. 37 (3) (2019) 3211–3218.
[33] Y. Wu, Q. Lv, X. Wu, X. Wang, L. Chen, K. Cen, Simultaneous measurement of surface tension and viscosity of oscillating droplet using time-resolved rainbow refractometry, Powder Technol. 391 (2021) 425–431.
[34] Q. Lv, Y. Wu, C. Li, X. Wu, L. Chen, K. Cen, Surface tension and viscosity measurement of oscillating droplet using rainbow refractometry, Opt. Lett. 45 (24) (2020) 6687–6690.
[35] C. Li, X. Wu, J. Cao, L. Chen, G. Gréhan, K. Cen, Application of rainbow refractometry for measurement of droplets with solid inclusions, Optic. Laser Technol. 98 (2018) 354–362.
[36] P. Walters, Optical measurement of water droplets in wet steam, Wet Steam 4 (1973) 32–40.
[37] D.K. Agarwal, A. Vaidyanathan, S.S. Kumar, Synthesis and characterization of kerosene–alumina nanofluids, Appl. Therm. Eng. 60 (1–2) (2013) 275–284.
[38] A. Macke, M.I. Mishchenko, Applicability of regular particle shapes in light scattering calculations for atmospheric ice particles, Appl. Opt. 35 (21) (1996) 4291–4296.
[39] S. Saengkaew, T. Charinpanitkul, H. Vanisri, W. Tanthapanichakoon, L. Mees, G. Gouesbet, G. Gréhan, Rainbow refractrometry: on the validity domain of Airy's and Nussenzveig's theories, Optic. Commun. 259 (1) (2006) 7–13.
[40] A.H. Harvey, J.S. Gallagher, J.L. Sengers, Revised formulation for the refractive index of water and steam as a function of wavelength, temperature and density, J. Phys. Chem. Ref. Data 27 (4) (1998) 761–774.
[41] L. Rayleigh, On the instability of jets, Proc. London Math. Soc. 1 (1) (1878) 4–13.